



## OPEN ACCESS

## EDITED BY

Sergei Manzhos,  
National University of Singapore,  
Singapore

## REVIEWED BY

Minglei Sun,  
King Abdullah University of Science and  
Technology, Saudi Arabia  
Michael Nolan,  
University College Cork, Ireland

## \*CORRESPONDENCE

Koichi Yamashita,  
yamashita@chemsys.t.u-tokyo.ac.jp

## SPECIALTY SECTION

This article was submitted to Solar  
Energy,  
a section of the journal  
Frontiers in Energy Research

RECEIVED 30 April 2022

ACCEPTED 27 September 2022

PUBLISHED 12 October 2022


## CITATION

Kaneko M, Nozawa S and Yamashita K  
(2022), Electron-phonon interaction  
and structural changes in the  
electronically excited state of  
WO<sub>3</sub> photocatalyst.  
*Front. Energy Res.* 10:933044.  
doi: 10.3389/fenrg.2022.933044

## COPYRIGHT

© 2022 Kaneko, Nozawa and Yamashita.  
This is an open-access article  
distributed under the terms of the  
[Creative Commons Attribution License  
\(CC BY\)](#). The use, distribution or  
reproduction in other forums is  
permitted, provided the original  
author(s) and the copyright owner(s) are  
credited and that the original  
publication in this journal is cited, in  
accordance with accepted academic  
practice. No use, distribution or  
reproduction is permitted which does  
not comply with these terms.

# Electron-phonon interaction and structural changes in the electronically excited state of WO<sub>3</sub> photocatalyst

Masanori Kaneko<sup>1</sup>, Shunsuke Nozawa <sup>2</sup> and  
Koichi Yamashita<sup>1\*</sup>

<sup>1</sup>Element Strategy Initiative for Catalysts and Batteries (ESICB), Kyoto University, Kyoto, Japan, <sup>2</sup>Photon Factory, Institute for Materials Structure Science, KEK, Tsukuba, Japan

The structural changes in the electronically excited state of tungsten oxide (WO<sub>3</sub>), a promising visible-light-responsive photocatalyst, are discussed from the viewpoint of carrier-phonon interactions using first-principles calculations. The increase in the pre-edge peak observed immediately after photoexcitation by high-speed time-resolved X-ray absorption spectroscopy is attributed to the local lattice distortion due to Fröhlich-Polaron generation by the interaction with optical longitudinal phonons. Bimolecular recombination could be suppressed by the formation of bipolaron states, and high internal quantum yields in photocatalysis are expected. The bipolaron states are unstable states in the electronically excited state, and relax to stable structures in the electronically excited state by phonon-phonon interaction. In the stable structure, the transition dipole moment is found to be nearly zero, suggesting a non-radiative transition to the electronic ground state and a long lifetime in the electronically excited state.

## KEYWORDS

electron-phonon interaction, Fröhlich-Polaron, electronically excited state, WO<sub>3</sub> photocatalyst, density functional theory

## 1 Introduction

Photocatalysts, which utilize sunlight to extract hydrogen and oxygen from water, is an essential technology for realizing a sustainable and clean society (Kamat, 2007). In a photocatalytic reaction, when the photocatalyst absorbs light, the electrons are excited, and electron-hole pairs are generated; subsequently, they move away from each other and ultimately reach the surface to proceed with the reaction with the adsorbed substance (Kisch, 2015). This technology is one of the leading technologies in the development of renewable energy (Kudo and Miseki, 2009), and it is expected that the photocatalytic function will be improved by elucidating the reaction process. Thus far, research and development of photocatalysts were centered on titanium oxide (TiO<sub>2</sub>) that responds to ultraviolet light (Ameta and Ameta, 2017); however, the amount of ultraviolet light contained in sunlight is about 5% of the total, so it is essential to develop a catalytic

material that absorbs visible light and promotes the reaction in order to ensure the effective use of sunlight (Maeda and Domen, 2010).

Tungsten trioxide ( $\text{WO}_3$ ), with a bandgap of 2.6–2.8 eV, has been noted as a visible light-responsive photocatalytic material (Kiu et al., 2012), and research has been conducted on the dynamics of photoexcited states and photocarriers. By light irradiation, electrons in the valence band of the 2p orbital of oxygen are excited to the conduction band of the 5d orbital of Tungsten to generate optical carriers (Niklasson and Granqvist, 2007). Regarding the lifetime of optical carriers in  $\text{WO}_3$ , it has been reported that more than 90% of photogenerated electron-holes recombine within 10  $\mu\text{s}$  (Pesci et al., 2011). However, long-lived optical carriers with a lifetime of 100  $\mu\text{s}$  or more have been observed in the  $\text{WO}_3$  fine particles, and it has been confirmed that they have important properties that cannot be ignored as a photocatalyst (Amano et al., 2013). Regarding the structure of the photocarrier and the size dependence of the material, a high photocurrent of  $\sim 2.4 \text{ mA cm}^{-2}$  was observed with the monoclinic nanoneedle  $\text{WO}_3$  (Fàbrega et al., 2016), and it has been reported that the life of charge carriers is longer in nano-sized powders compared to granular powders  $390 \pm 260 \text{ nm}$  (Regan et al., 2016).

In contrast, there was a lack of information on the structural changes in the electronic excitation state generated by the  $\text{WO}_3$  photocatalyst under light irradiation. However, Asakura et al. followed the structural changes in the photoexcited state of  $\text{WO}_3$  by ultrafast time-resolved X-ray absorption spectroscopy at the W-LI, -LIII edges, and succeeded in observing local structural changes of photoexcited  $\text{WO}_3$  on an ultrafast atomic scale (Uemura et al., 2014; Uemura et al., 2016; Koide et al., 2020). At the W-LI end, a chemical shift in the absorption spectrum due to the decrease in the oxidation number of W associated with the electronic excitation from the oxygen 2p orbital to the W d( $E_g$ ) orbital in the valence band was observed with a time resolution of 0.5 ps in the experiment. The increase in the intensity of the W-LI pre-edge peak due to the p-d hybridization effect originating from the local structural distortion around W was observed to continue up to 150 ps, i.e., the fraction of sites where the local structural distortion occurs increased up to 150 ps. By full-potential multiple scattering calculation, the anisotropic and local distortion around the W atom reproduces the characteristics of the spectrum 150 ps after photoexcitation (Koide et al., 2020). In the future, it is expected that research will be developed to track the chemical state and the structural changes during the photocatalytic reaction under light irradiation.

In this study, the structural changes in the electronically excited state caused by the light irradiation of  $\text{WO}_3$  in relation to the femtosecond time-resolved X-ray absorption fine structure (XAFS) spectroscopy experiment by Asakura et al. are discussed, based on the first-principles calculation method on the density functional theory. In particular, the structural changes induced immediately after light irradiation are clarified from the viewpoint of electron-photon interaction, followed by a discussion of the relaxation process to a stable structure in the electronically excited state. This study provides insight into the

dynamics of photogenerated carriers in  $\text{WO}_3$  and may contribute to the design of more efficient  $\text{WO}_3$ -based photocatalysts.

## 2 Method of calculations

The structure of the cubic phase  $Pm\bar{3}m$  (4 atomic system) was used for the calculation of the electronic state, phonon dispersion, and electron-phonon coupling. Brillouin zone integration, structural relaxation, and phonon calculations were performed on  $8 \times 8 \times 8$  k-point grid, whereas PDOS, and band structures on a  $16 \times 16 \times 16$  k-point grid. Phonon calculations were also conducted on a  $4 \times 4 \times 4$  q-point grid. The effective mass was calculated considering spin-orbit coupling (SOC). The calculation of the electronically excited state structure was done by utilizing a structure obtained by multiplying the structure of the monoclinic phase  $P2_1/n$  by  $2 \times 2 \times 2$  (equivalent to 256 atomic system,  $4 \times 4 \times 4$  super cell of cubic phase  $Pm\bar{3}m$ ). In the excited state calculation, the excited state configuration of the VBM electron excited to the CBM is represented by the constrained-occupation DFT (Gali et al., 2009). Integration of the Brillouin zone was performed on k-points with only  $\Gamma$ -points. Band unfolding has been performed using the BandUP 3.0.0-beta.6 software (Medeiros et al., 2014; Medeiros et al., 2015).

Quantum ESPRESSO 6.3 (Giannozzi et al., 2009) and Yambo 4.2.5 (Marini et al., 2009; Sangalli et al., 2019) were used for first-principles calculations based on density functional theory. The exchange correlation energies were approximated by generalized-gradient approximation (GGA) (Hua et al., 1997) and the functional (Perdew et al., 1996) defined by Perdew, Burke & Ernzerhof was used. Optimized norm-conserving Vanderbilt pseudopotentials (Hamann, 2013; van Setten et al., 2018) was used as the pseudopotential. The fully relativistic pseudopotential was used only for the calculation of the effective mass, whereas the others used the scalar relativistic pseudopotential. Structural optimization was performed so that the force applied to the atom was  $10^{-3}$  a. u. Or less and the stress was 0.1 kbar or less. The kinetic-energy cutoffs for the plane wave basis and charge density were 84 Ry and 336 Ry, respectively. VESTA (Momma and Izumi, 2011) and XCrySDen (Kokalj, 2003) were used to draw vectors such as structures and forces.

## 3 Results and discussions

### 3.1 Electronic structure

$\text{WO}_3$  is known to be in the monoclinic phase  $P2_1/n$  at room temperature and not in the cubic phase  $Pm\bar{3}m$  (Locherer et al., 1999; Vogt et al., 1999; Howard et al., 2001). However, because the electron-photon calculation in the monoclinic phase  $P2_1/n$  is extremely expensive, the structure of cubic phase  $Pm\bar{3}m$  was used.

TABLE 1 Effective mass of cubic phase  $Pm\bar{3}m$  CBM in units of the free electron mass  $m_0$ .

k point	Effective mass of CBM		
	$m^*$	$b$	$m^*(b = 0)$
$\Gamma \rightarrow M$	0.202	2.184	0.265
$\Gamma \rightarrow R$	0.246	0.667	0.280
$\Gamma \rightarrow X$	0.433	6.248	0.531
$X \rightarrow M$	0.169	0.487	0.178
$X \rightarrow R$	0.169	0.580	0.189

From the band structure (Supplementary Figure S1), it was found that the CBM is  $\Gamma$  (X is almost the same energy level as  $\Gamma$  without SOC), VBM is M or R, and bandgap is indirect. The bandgap is 0.65 eV without SOC, and 0.47 eV with SOC. For comparison we calculated the bandgap for the monoclinic phase  $P2_1/n$  and obtain 1.44 eV without SOC and 1.34 eV with SOC. The theoretical bandgaps are smaller than the experimental bandgap of 2.60–3.21 eV (González-Borrero et al., 2010; Migas et al., 2010; Zheng et al., 2011) for monoclinic phase  $P2_1/n$ . This can be attributed to the underestimation of the bandgap due to the use of the functional PBE and the fact that the bandgap by first principles calculation is larger for the monoclinic phase  $P2_1/n$  than for the cubic phase  $Pm\bar{3}m$  (Wang et al., 2011; Hamdi et al., 2016; Yang et al., 2019). As will be discussed later, unfolding the band structure of the structure optimized with monoclinic phase  $P2_1/n$  as the initial structure to cubic phase  $Pm\bar{3}m$  shows little difference in band structure. From PDOS (Supplementary Figure S2), it was found that the VB and CB are made up of O (p) and W (d) orbitals, respectively.

The band structure was fitted with the following equation to calculate the effective mass.

$$\frac{\hbar^2 |\mathbf{k}|^2}{2m^*} = \epsilon_{\mathbf{k}} (1 + b\epsilon_{\mathbf{k}})$$

Recent studies have shown that the effective mass of  $\Gamma$ -X is a very small value,  $m^* = 0.17$ , when calculated with spin-orbit coupling (SOC) (Wang et al., 2020). Therefore, in this study, SOC was considered for the calculation of effective mass. It can be seen that the effective mass is relatively large with the VB approximately 0.9–2.4 (Supplementary Table S1) and small with the CB approximately 0.2–0.4 (Table 1).

### 3.2 Phonon and electron-phonon coupling

The phonon band and phonon DOS were calculated for the electron-phonon interaction analysis (Supplementary Figures S3, S4). The stable structure in the ground state is the monoclinic

phase  $P2_1/n$  and not the cubic phase  $Pm\bar{3}m$ , so a mode in which the frequency is imaginary appears, however it does not affect the following discussion. Two longitudinal optical (LO) modes appearing at  $\mathbf{q} = \Gamma$ , 386.8  $\text{cm}^{-1}$  ( $\nu = 9$ ) and 877.2  $\text{cm}^{-1}$  ( $\nu = 12$ ), are called LO1 and LO2, respectively. The phonon DOS indicate that they are modes of O atoms. The appearance of imaginary frequency modes and LO modes have also been reported in previous studies (Yang et al., 2019; Wang et al., 2020).

Electron-phonon spectral density  $\alpha^2 F(\omega)$  (Giustino, 2017) was calculated in order to confirm the magnitude of electron-phonon interaction in the VB and CB. It represents the scattering of an electron on the Fermi surface and cannot be applied to semiconductors with band gaps as is. Therefore, the Fermi energy of the electron-phonon spectral density was replaced with an arbitrary energy  $\epsilon_A$ , and it could be applied in an arbitrary energy region.

$$\alpha^2 F(\omega; \epsilon_A) = \frac{1}{N(\epsilon_A)} \int \frac{d\mathbf{k}d\mathbf{q}}{\Omega_{\text{BZ}}^2} \sum_{i,j,\nu} |g_{ij,\nu}(\mathbf{k}, \mathbf{q})|^2 \delta(\epsilon_{i\mathbf{k}} - \epsilon_A) \delta(\epsilon_{j\mathbf{k}+\mathbf{q}} - \epsilon_A) \delta(\hbar\omega - \hbar\omega_{q\nu})$$

where  $g_{ij,\nu}(\mathbf{k}, \mathbf{q})$  is an electron-phonon matrix element, with  $\nu$  being the phonon branch index and  $\mathbf{k}$  being k-point and  $\mathbf{q}$  being the phonon wave vector and  $i, j$  being the band indices, and  $\epsilon_{i\mathbf{k}}$ ,  $\epsilon_{j\mathbf{k}+\mathbf{q}}$  are the energies of the Bloch state, and  $\omega_{q\nu}$  is the phonon frequency, and  $\epsilon_A$  is an arbitrary energy.

Figure 1 shows the results of the calculation of  $\alpha^2 F$  near the VBM and CBM, where  $\epsilon_A$  is VBM or CBM. In both cases, the mode of  $\nu = 9, 12$  has a large peak. The electron-phonon matrix element in Figure 2A indicates that both  $\nu = 9$  and 12 become 0 at the  $\Gamma$  point, but increases while approaching  $\mathbf{q} = \Gamma$  point. As the vicinity of the  $\mathbf{q} = \Gamma$  point of  $\nu = 9, 12$  is LO1 and LO2, it can be seen that both vibrational modes are strongly coupling with the electrons near the  $\mathbf{q} = \Gamma$  point. Therefore, we focus only on the electron-phonon coupling at the  $\mathbf{q} = \Gamma$  point. Figures 2B,C shows the vibrational modes of LO1 and LO2 at the point  $\mathbf{q} = \Gamma$ . As shown in phonon DOS, it can be seen that they both correspond to the vibration in the plane of the O atom.

### 3.3 Fröhlich polarons

It is known that polar perovskite materials form Fröhlich polarons by the interaction of photogenerated carriers (electrons, holes) and longitudinal optical phonons (Fröhlich, 1954). It has been pointed out that polaron diffusion of photogenerated carriers is a factor contributing the high efficiency of methylammonium lead (MAPb) halide perovskite solar cells (Ghosh et al., 2020). Zhu et al. reported that Fröhlich polarons were generated at 0.3 ps in MAPbI<sub>3</sub> (Miyata and Zhu, 2018), and 0.7 ps for CsPbBr<sub>3</sub> after light irradiation (Cinquanta et al., 2019). The observed high defect tolerance is also explained by the formation of Fröhlich polarons (Miyata and

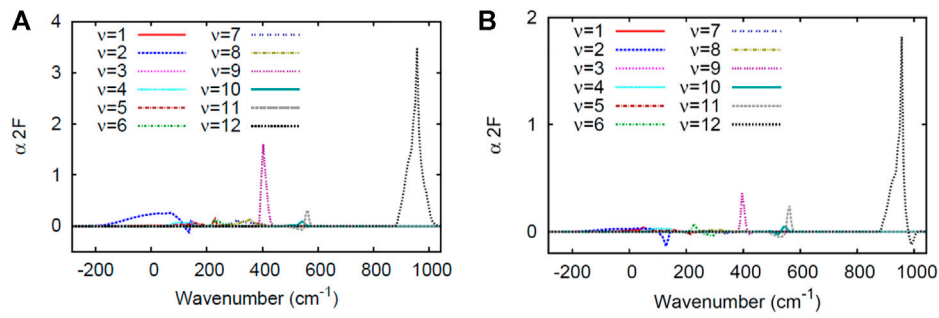


**FIGURE 1** Electron-phonon spectral density  $\alpha^2 F$  of cubic phase  $Pm\bar{3}m$ . Mode  $v$  is assigned in an ascending order. (A)  $\epsilon_A = \epsilon_{VBM} - \delta$  (B)  $\epsilon_A = \epsilon_{CBM} + \delta$ ,  $\delta = 0.02$  Ry.

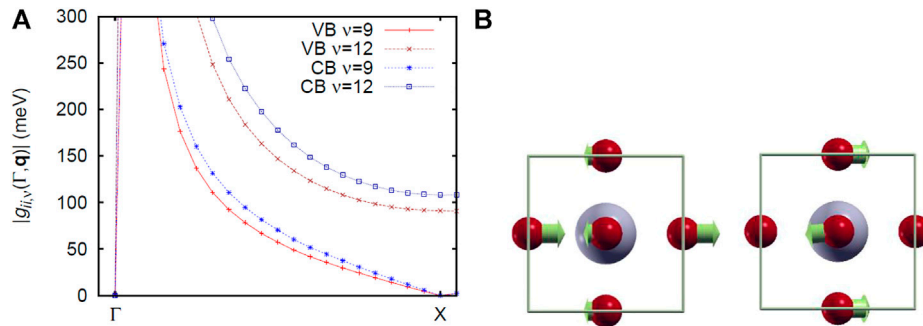


**FIGURE 2** Cubic phase  $Pm\bar{3}m$ , (A) electron-phonon matrix elements for LO vibrational modes, (B) LO1 ( $v = 9$ ,  $q = \Gamma$ ) (C) LO2 ( $v = 12$ ,  $q = \Gamma$ ).

Zhu, 2018). The interaction between electron and hole polarons is expected to be repulsive when the lattice distortion associated with polaron formation is large, because the Coulomb interaction between electrons and holes is shielded by the large dielectric constant of ferroelectric perovskites (Emin, 2018). Thus, the repulsive interaction between electron and hole polarons is thought to suppress bimolecular recombination and allow carriers to diffuse over long distances.

The Fröhlich constant  $\alpha_F$ , which indicates the coupling strength of Fröhlich polaron, is expressed by Feynman’s Fröhlich-Hamiltonian-based path integral variational method (Feynman, 1955).

$$\alpha_F = \frac{e^2}{\hbar} \left( \frac{1}{\epsilon_\infty} - \frac{1}{\epsilon_0} \right) \sqrt{\left( \frac{m}{2\hbar\omega} \right)} \quad (1)$$

Here,  $\epsilon_\infty$  is the optical permittivity,  $\epsilon_0$  is the electrostatic permittivity,  $m$  is the effective band mass, and  $\hbar\omega$  is the frequency of the LO phonon.

From the calculation result of electron-phonon spectral density for  $WO_3$  in the previous section, the photogenerated

**TABLE 2** Fröhlich constant  $\alpha_F$ , effective mass  $m_p$ , radius  $r_p$ , lifetime  $\tau_B$ , and mobility  $\mu_B$  of electron- and hole-polarons.

	Electron-polaron		Hole-polaron	
	LO1	LO2	LO1	LO2
$\alpha_F$	0.68	1.02	1.74	2.62
$m_p$	0.26	0.28	2.28	2.99
$r_p$ ( $10^{-8}$ m)	3.14	1.42	1.99	0.87
$\tau_K$ (ps)	1.84	0.25	0.71	0.09
$\mu_H$ ( $cm^2/V \cdot s$ )	643	146	30	6

electrons and holes strongly interact with the longitudinal optical phonons (LO1, LO2) near the upper edge of the VB and the lower edge of the CB, respectively. Table 2 shows the Fröhlich constant  $\alpha_F$  calculated by Eq. 1. For the band effective mass, 0.216 (CBM) and 1.42 (VBM), which are the harmonic means of the electrons and hole effective masses in Table 1 and Supplementary Table S1,

were used; for  $\epsilon_{\infty}$  and  $\epsilon_0$ , the theoretically calculated values [ (Ping et al., 2013), (Feynman et al., 1962)] were used. The Fröhlich constants of the electron-polaron by LO1 and LO2 were obtained as 0.68 and 1.02, and those of the hole-polaron as 1.74 and 2.62, respectively. Because the Fröhlich polaron generation conditions are  $1 < \alpha_F < 6$ , it is considered that the photogenerated electrons and holes could produce electrons-polarons and hole-polarons having distorted lattice deformation with locally shifted oxygen atoms. As described in Chapter III-1, it is believed that the formation of Fröhlich polarons suppresses electron-hole bimolecular recombination, and it is expected that a highly efficient internal quantum yield of photocatalysis for defect-free  $\text{WO}_3$ .

The temperature dependence of the effective mass, radius, and mobility of the Fröhlich polaron is formulated by Feynman in a model of a simplified effective mass band structure that interacts with the continuum dielectric of the characteristic response frequency (Feynman, 1955; Feynman et al., 1962). Forst (Frost, 2017a) variationally solved the Feynman polaron model (Feynman, 1955) at a finite temperature (Feynman et al., 1962), and from the obtained variational parameters, developed a custom code to calculate the lifetime of polaron by Kadanoff's method (Kadanoff, 1963) and the mobility of polaron by Hellwarth et al. (Hellwarth and Biaggio, 1999); this is published in a GitHub repository (Frost, 2017b). Table 2 shows the effective mass  $m_p$  of the polaron, radius  $r_p$ , and Kadanoff lifetime  $\tau_K$  and Hellwarth mobility  $\mu_H$  at room temperature calculated by Forst's method (Frost, 2017a; Frost, 2017b).  $\text{WO}_3$  as a photocatalyst material is considered to be a promising material from the viewpoint of the mobility of the electron- and hole-polarons which are generated by interaction with LO1. In addition, W. Wang et al. predicted the electron mobility at room temperature by the first-principles calculation using the Boltzmann transport theory for the transport characteristics of  $\text{WO}_3$ , and the same tendency as  $485 \text{ cm}^2/\text{Vs}$  with  $1,020 \text{ cm}^{-3}$  doping (Wang et al., 2020). The very long electron mobility is expected to allow  $\text{WO}_3$  to be used effectively as an electron transport layer in high-efficiency solar cells.

Unfortunately, in the current first-principles calculation technology, and structural optimization of the bipolaron state (an electron-polaron and a hole-polaron coexist) with local lattice distortion is almost impossible even with the Bethe-Salpeter equation method considering the electron-hole interaction. Bousquet et al. calculated the self-trapped single-electron polaron in  $\text{WO}_3$  from density functional theory (Bousquet et al., 2020). The calculations concluded that the single polaron is at a higher energy than the fully delocalized solution and is an excited state of  $\text{WO}_3$ . The shape of the density distribution corresponds to the shape of the  $W\text{-}d_{xy}$  orbital with four lobes oriented towards the oxygen bond, consistent with the CBM of  $\text{WO}_3$ . Moreover, because the  $d_{xy}$  orbital extends in two directions ( $xy$ ), the polaron formed by the entry of electrons into

this  $d_{xy}$  orbital shows a two-dimensional shape; and spin density showed that the charge of the polaron was localized in the  $xy$  plane of  $\text{WO}_3$  and did not spread to other atomic planes along the  $z$  direction. This disk-shaped electron density distribution has also been proposed from the ESR measurement of the single-electron polaron of  $\text{WO}_3$  (Salje, 1994).

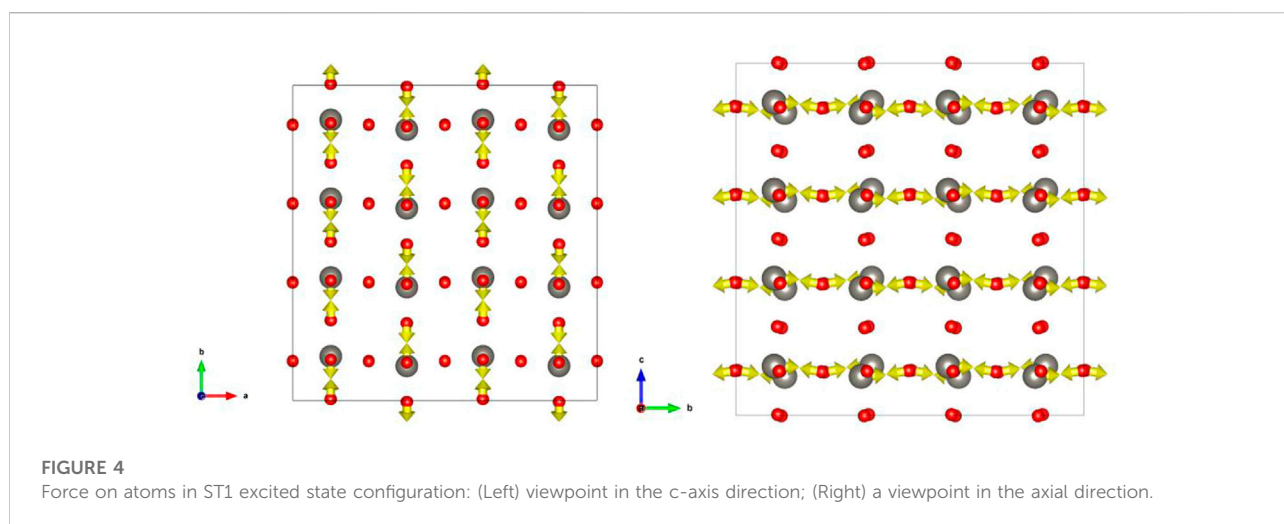
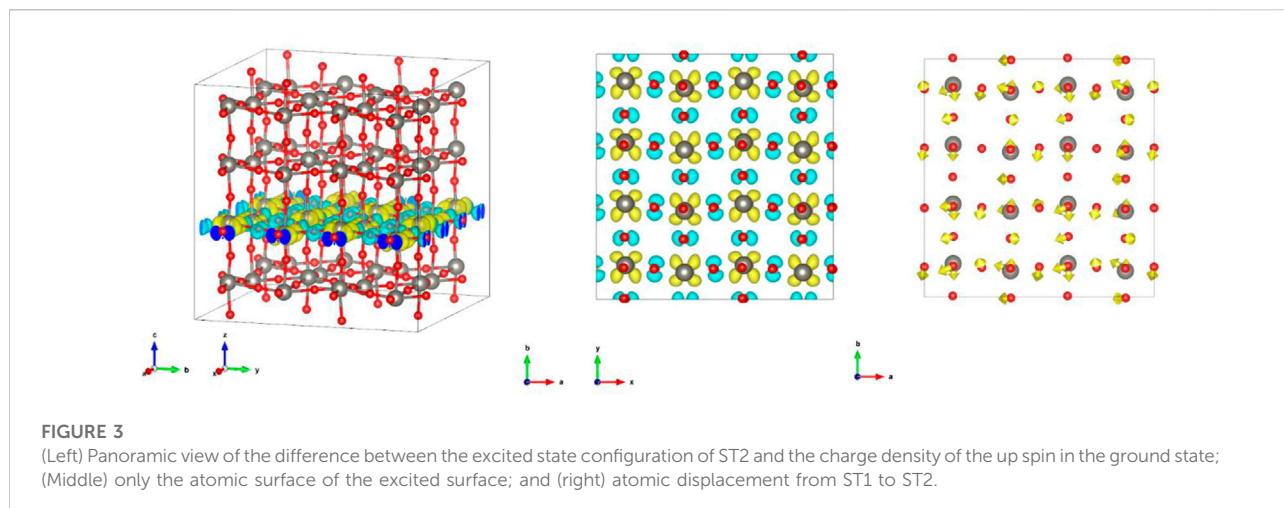
Ultrahigh-speed time-resolved X-ray absorption spectra (Uemura et al., 2014; Uemura et al., 2016; Koide et al., 2020) by Asakura et al. have been interpreted as indicating that light irradiation induces local structural changes around W, with an increasing fraction of sites undergoing local structural distortion up to 150 ps. From the above calculation results, it is suggested that the local structural change after light irradiation is derived from the lattice distortion due to the formation of Fröhlich polaron.

### 3.4 Excited state configurations

The widely used method for describing the excited state of a solid by considering electron-hole interaction is a combination of the GW approximation (Hedin, 1965) and the Bethe-Salpeter equation (Salpeter and Bethe, 1951). However, this method is difficult to use in the calculation of large systems that may undergo localized structural changes, such as those used in this study. Therefore, we used the constrained occupation DFT method (Gali et al., 2009), which is a commonly used DFT-based method with low computational cost. In constrained occupied DFT, the total energy of the excited state configuration is approximated by the DFT total energy of the Kohn-Sham system. Where one of the occupied Kohn-Sham states drops out and a higher unoccupied Kohn-Sham state is occupied. In this study, an electron in the VBM was unoccupied and occupied by the CBM. During the self-consistent calculation of the Kohn-Sham equation, the constrained occupancy of the orbitals is fixed. In this method, the total energy is clearly defined, so that the structure of the system can be optimized.

First, the monoclinic  $P2_1/n$  ( $2 \times 2 \times 2$  times cubic phase  $Pm\bar{3}m$ , 32 atomic system) was relaxed with a structure (256 atomic system) multiplied by  $2 \times 2 \times 2$ . The initial structure was a monoclinic  $P2_1/n$  (Woodward et al., 1995) reported by Woodward et al., but the relaxed structure was a triclinic  $P\bar{1}$ . From now on, this structure will be referred to as ST1. Triclinic  $P\bar{1}$  has been reported for structures cooler than room temperature (González-Borrero et al., 2010), and is reported to be the most stable in DFT calculations (Hamdi et al., 2016). The tolerance for the identification of the space group was performed at  $10^{-3} \text{ \AA}$ . For this ST1, constrained was applied to the occupations and only the atomic position was relaxed in the excited state configuration. The space group became triclinic  $P\bar{1}$ . From now on, this structure will be referred to as ST2.



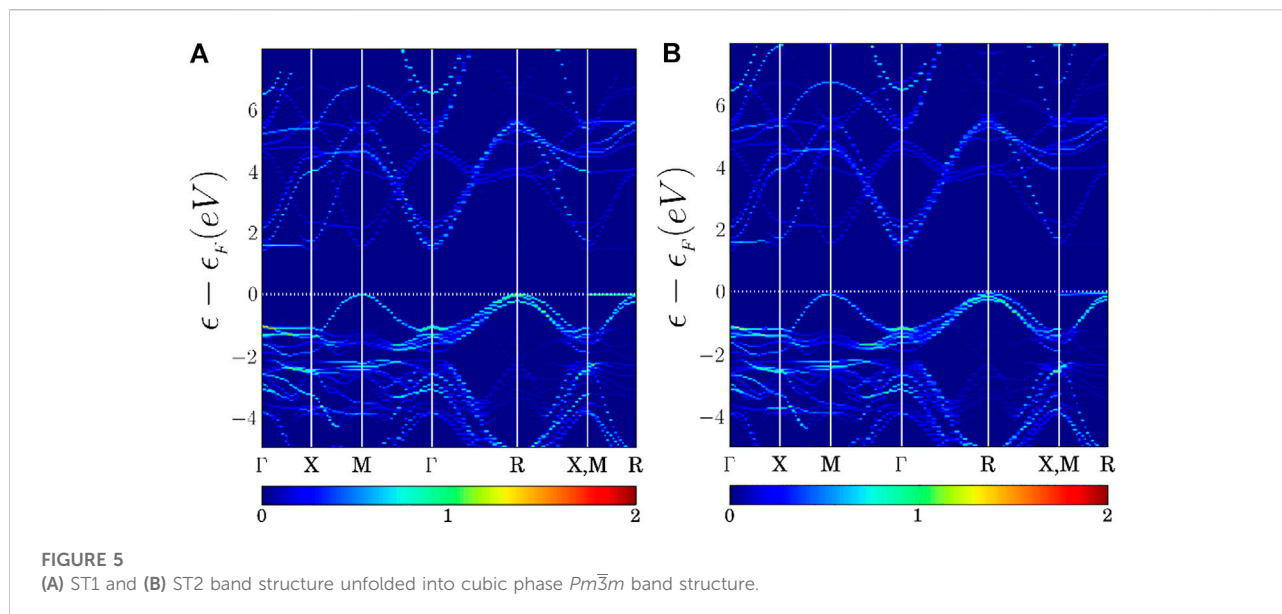


Observing the difference between the excited state configuration of ST2 and the charge density of the ground state (Figures 3A,B), it can be seen that the electron of one of O (p) atom on  $\text{WO}_2$  surface is excited to W (d). The charge densities of the CB and VB of ST1 (Supplementary Figures S5, S6) are both spread three-dimensionally throughout the crystal. This suggests that the electronic states of the CBM and VBM are separated into each surface due to the structural change in the excited state configuration.

Observing the displacement of atoms from ST1 to ST2 (Figure 3C), it can be seen that the W atom is displaced in the direction of the O atom in the excited state. This seems to correspond to the movement of the W atom in previous studies. In particular, the displacement of the W atom was moved in the direction of reducing the zigzag of the zigzag-W-O-W-O-chain. It was found that the O atom does not displace in the direction of the W atom. It can be seen from the distance between the W atom

and the O atom near the n-th neighbor (Supplementary Table S2) that the W-O bonds near the 3<sup>rd</sup> and 4<sup>th</sup> neighborhood, which were originally almost equidistant, became shorter on one side and longer on the other side due to the structural change in the excited state. Similarly, when calculating the distance between W-O atoms for the structure shifted in the direction of force that was applied in the electronically excited state of ST1, it can be seen that, unlike the previous case, the W-O bond in the vicinity of the second neighborhood becomes longer, and the W-O bond in the vicinity of the 4<sup>th</sup> and 5<sup>th</sup> neighborhoods becomes shorter. In other words, it is suggested that the direction of the force that the atom receives are different at the beginning of the electronically excited state and when the structure finally becomes stable in the excited state configuration.

Figure 4 shows the force applied to the atom in the excited state configuration of ST1. Observing this, it can be seen that the W atom also tends to be displaced toward the O atom. As the



displacement to the triclinic  $P1$  in the excited state (Figure 3C) shows the same direction, it can be seen that the W atom continues to move to the O atom. In contrast, the O atom tries to displace in the direction of the W atom, but seems to move in the other direction from the middle.

Figure 5 shows the band structure of ST1 and ST2 unfolded into the band structure of cubic phase  $Pm\bar{3}m$ . On comparison with the band diagram of cubic phase  $Pm\bar{3}m$  (Supplementary Figure S1), it can be seen that there is no significant change. The absolute value of the dipole matrix elements between the VBM and CBM was almost zero in both ST1 and ST2. From these facts, it is considered that what was originally an indirect gap in the cubic phase  $Pm\bar{3}m$  is maintained as it is in ST1 and ST2.

An increase in pre-edge peak was observed immediately after photoexcitation in Asakura et al. The W-LI edge-time-resolved X-ray absorption spectroscopy (Koide et al., 2020) can be attributed to the increase in p-d hybrids due to orthorhombic local structural changes by Fröhlich polarons. In addition, the measured W-LI pre-edge peak intensity kinetics showed that the proportion of sites with orthorhombic local structure increased from the photoexcitation to 150 ps; and it can be understood that after 150 ps, we are observing a gradual return to the original monoclinic structure.

## 4 Conclusion

In this study, the structural change of  $WO_3$  in the electronic excited state was discussed by first-principles calculation from the viewpoint of carrier phonon interaction. The increase in pre-edge peaks immediately after photoexcitation observed by the ultrafast time-resolved X-ray absorption spectroscopy was discussed from the local structural changes due to Fröhlich polaron generation owing to

their interaction with the optical vertical phonons. Therefore, in defect-free  $WO_3$ , bimolecular recombination could be suppressed by the formation of bipolaron states, and high internal quantum yields in photocatalysis are expected. A detailed study of the defect structure is needed to further increase the quantum yield of  $WO_3$  in photocatalysis. The bipolaron state of the electronic polaron and hole polaron is an unstable state in the electronic excitation state, and is relaxed to a stable structure in the electronic excitation state by phonon-phonon interaction. The gradual increase in W-LI pre-edge peak intensity up to 150 ps indicates an increase in the proportion of sites with local structural changes due to Fröhlich polaron formation. In the stable structure, the electron and hole are delocalized at the top of the conduction band and the valence band, respectively. However, the transition dipole moment is indirectly transitional and almost zero. As observed by the ultra-high-speed time-resolved X-ray absorption spectroscopy experiment, it is considered that there is no radiation transition from the stable structure of the electronically excited state to the ground state with a relaxation time of 1800 ps.

However, the above discussion is based on the result of the electronic state theory in one electron approximation, and hence is quantitatively insufficient. In particular, the introduction of the Bethe-Salpeter method, which considers the electron-hole pair interaction, is indispensable for describing the excited state in which the electron-hole pair exists. Moreover, to describe the polaron state, band calculation in a very large supercell is required.

On the other hand, some important issues remain to be solved, such as the microscopic mechanism of hot excitons to Fröhlich polaron formation in the early stage of photoexcitation, the interaction between electron polaron and hole polaron, and the competitive mechanism between carrier conduction and local structural change, and theoretical studies to elucidate these issues are planned in the future.

## Data availability statement

The original contributions presented in the study are included in the article/Supplementary Material, further inquiries can be directed to the corresponding author.

## Author contributions

MK and KY performed the DFT calculation. All authors discussed the results and commented on the manuscript. KY supervised the project.

## Funding

This research was supported by JSPS KAKENHI in Scientific Research on Innovative Areas “Innovations for Light-Energy Conversion (<sup>14</sup>LEC)”, and by MEXT as “Program for Promoting Researches on the Supercomputer Fugaku” (Realization of innovative light energy conversion materials utilizing the supercomputer Fugaku, JPMXP1020210317) KY acknowledges the support from Toyota Physical and Chemical Research Institute. The computations were performed at the Research Center for Computational Science, Okazaki, Japan (Project: 22-IMS-C039).

## Conflict of interest

The authors declare that the research was conducted in the absence of any commercial or financial relationships that could be construed as a potential conflict of interest.

## References

- Amano, F., Ishinaga, E., and Yamakata, A. (2013). Effect of particle size on the photocatalytic activity of WO<sub>3</sub> particles for water oxidation. *J. Phys. Chem. C* 117, 22584–22590. doi:10.1021/jp408446u
- Ameta, R., and Ameta, S. C. (2017). *Photocatalysis: Principles and applications*. Boca Raton: CRC Press.
- Bousquet, E., Hamdi, H., Aguado-Puente, P., Salje, E. K. H., Artacho, E., and Ghosez, P. (2020). First-principles characterization of single-electron polaron in WO<sub>3</sub>. *Phys. Rev. Res.* 2, 012052. doi:10.1103/physrevresearch.2.012052
- Cinquanta, E., Meggiolaro, D., Motti, S. G., Gandini, M., Alcocer, M. J. P., Akkerman, Q. A., et al. (2019). Ultrafast THz probe of photoinduced polarons in lead-halide perovskites. *Phys. Rev. Lett.* 122 (16), 166601. doi:10.1103/physrevlett.122.166601
- Emin, D. (2018). Barrier to recombination of oppositely charged large polarons. *J. Appl. Phys.* 123, 055105. doi:10.1063/1.5019834
- Fàbrega, C., Murcia-López, S., Monllor-Satoca, D., Prades, J. D., Hernández-Alonso, M. D., Penelas, G., et al. (2016). Efficient WO<sub>3</sub> photoanodes fabricated by pulsed laser deposition for photoelectrochemical water splitting with high faradaic efficiency. *Appl. Catal. B Environ.* 189, 133–140. doi:10.1016/j.apcatb.2016.02.047
- Feynman, R. P., Hellwarth, R. W., Iddings, C. K., and Platzman, P. M. (1962). Mobility of slow electrons in a polar crystal. *Phys. Rev.* 127, 1004–1017. doi:10.1103/physrev.127.1004
- Feynman, R. P. (1955). Slow electrons in a polar crystal. *Phys. Rev.* 97 (3), 660–665. doi:10.1103/physrev.97.660
- Frost, J. M. (2017). Available at.
- Frost, J. M. (2017). Calculating polaron mobility in halide perovskites. *Phys. Rev. B* 96, 195202. doi:10.1103/physrevb.96.195202
- Frohlich, H. (1954). Electrons in lattice fields. *Adv. Phys.* X, 3 (11), 325–361. doi:10.1080/00018735400101213
- Gali, A., Janzén, E., Deák, P., Kresse, G., and Kaxiras, E. (2009). Theory of spin-conserving excitation of the N–V–Center in diamond. *Phys. Rev. Lett.* 103, 186404. doi:10.1103/physrevlett.103.186404
- Ghosh, D., Welch, E., Neukirch, A. J., Zakhidov, A., and Tretiak, S. (2020). Polarons in halide perovskites: A perspective. *J. Phys. Chem. Lett.* 11 (9), 3271–3286. doi:10.1021/acs.jpclett.0c00018
- Giannozzi, P., Baroni, S., Bonini, N., Calandra, M., Car, R., Cavazzoni, C., et al. (2009). Quantum ESPRESSO: A modular and open-source software project for quantum simulations of materials. *J. Phys. Condens. Matter* 21, 395502. doi:10.1088/0953-8984/21/39/395502
- Giustino, F. (2017). Electron-phonon interactions from first principles. *Rev. Mod. Phys.* 89, 015003. doi:10.1103/revmodphys.89.015003

## Publisher's note

All claims expressed in this article are solely those of the authors and do not necessarily represent those of their affiliated organizations, or those of the publisher, the editors and the reviewers. Any product that may be evaluated in this article, or claim that may be made by its manufacturer, is not guaranteed or endorsed by the publisher.

## Supplementary material

The Supplementary Material for this article can be found online at: <https://www.frontiersin.org/articles/10.3389/fenrg.2022.933044/full#supplementary-material>

### SUPPLEMENTARY FIGURE S1

Cubic phase  $Pm\bar{3}m$  band structure, (left) without SOC. (right) with SOC.

### SUPPLEMENTARY FIGURE S2

Cubic phase  $Pm\bar{3}m$  PDOS.

### SUPPLEMENTARY FIGURE S3

Phonon band.

### SUPPLEMENTARY FIGURE S4

Phonon DOS.

### SUPPLEMENTARY FIGURE S5

ST1 contribution of CB, CB+1, CB+2, CB+3 (1.442, 1.512, 1.512, 1.517 eV) wavefunctions to the charge density.

### SUPPLEMENTARY FIGURE S6

ST1 contribution of VB, VB+1, VB+2, VB+3 (0.000, -0.004, -0.004, -0.007 eV) wavefunctions to the charge density.

### SUPPLEMENTARY TABLE S1

Effective mass of cubic phase  $Pm\bar{3}m$  VBM in units of the free electron mass.

### SUPPLEMENTARY TABLE S2

Mean of distance between W atom and O atom near nth (Å).



- González-Borrero, P. P., Sato, F., Medina, A. N., Baesso, M. L., Bento, A. C., Baldissera, G., et al. (2010). Optical band-gap determination of nanostructured WO<sub>3</sub> film. *Appl. Phys. Lett.* 96, 061909. doi:10.1063/1.3313945
- Hamann, D. R. (2013). Optimized norm-conserving Vanderbilt pseudopotentials. *Phys. Rev. B* 88, 085117. doi:10.1103/physrevb.88.085117
- Hamdi, H., Salje, E. K. H., Ghosez, P., and Bousquet, E. (2016). First-principles reinvestigation of bulk WO<sub>3</sub>. *Phys. Rev. B* 94, 245124. doi:10.1103/physrevb.94.245124
- Hedin, L. (1965). New method for calculating the one-particle green's function with application to the electron-gas problem. *Phys. Rev.* 139, A796–A823. doi:10.1103/physrev.139.a796
- Hellwarth, R. W., and Biaggio, I. (1999). Mobility of an electron in a multimode polar lattice. *Phys. Rev. B* 60, 299–307. doi:10.1103/physrevb.60.299
- Howard, C. J., Luca, V., and Knight, K. S. (2001). High-temperature phase transitions in tungsten trioxide - the last word? *J. Phys. Condens. Matter* 14, 377–387. doi:10.1088/0953-8984/14/3/308
- Hua, X., Chen, X., and Goddard, W. A. (1997). Generalized gradient approximation: an improved density-functional theory for accurate orbital eigenvalues. *Phys. Rev. B* 55, 16103–16109. doi:10.1103/physrevb.55.16103
- Kadanoff, L. P. (1963). Boltzmann equation for polarons. *Phys. Rev.* 130, 1364–1369. doi:10.1103/physrev.130.1364
- Kamat, P. V. (2007). Meeting the clean energy Demand: nanostructure architectures for solar energy conversion. *J. Phys. Chem. C* 111, 2834–2860. doi:10.1021/jp066952u
- Kisch, H. (2015). *Semiconductor photocatalysis: Principles and applications*. Wiley VCH.
- Kiu, X., Wang, F., and Wang, Q. (2012). Nanostructure-based WO<sub>3</sub> photoanodes for photo-electrochemical water splitting. *Phys. Chem. Chem. Phys.* 14, 7894–7911. doi:10.1039/c2cp40976c
- Koide, A., Uemura, Y., Kido, D., Wakisaka, Y., Takakusagi, S., Ohtani, B., et al. (2020). Photoinduced anisotropic distortion as the electron trapping site of tungsten trioxide by ultrafast W L<sub>1</sub>-edge X-ray absorption spectroscopy with full potential multiple scattering calculations. *Phys. Chem. Chem. Phys.* 22, 2615–2621. doi:10.1039/c9cp01332f
- Kokalj, A. (2003). Computer graphics and graphical user interfaces as tools in simulations of matter at the atomic scale. *Comput. Mater. Sci.* 28, 155–168. doi:10.1016/s0927-0256(03)00104-6
- Kudo, A., and Miseki, Y. (2009). Heterogeneous photocatalyst materials for water splitting. *Chem. Soc. Rev.* 38, 253–278. doi:10.1039/b800489g
- Locherer, K. R., Swainson, I. P., and Salje, E. K. H. (1999). Phase transitions in tungsten trioxide at high temperatures - a new look. *J. Phys. Condens. Matter* 11, 6737–6756. doi:10.1088/0953-8984/11/35/312
- Maeda, K., and Domen, K. (2010). Photocatalytic water splitting: Recent progress and future challenges. *J. Phys. Chem. Lett.* 1, 2655–2661. doi:10.1021/jz1007966
- Marini, A., Hogan, C., Grüning, M., and Varsano, D. (2009). Yambo: An ab initio tool for excited state calculations. *Comput. Phys. Commun.* 180, 1392–1403. doi:10.1016/j.cpc.2009.02.003
- Medeiros, P. V. C., Stafström, S., and Björk, J. (2014). Effects of extrinsic and intrinsic perturbations on the electronic structure of graphene: Retaining an effective primitive cell band structure by band unfolding. *Phys. Rev. B* 89, 041407. doi:10.1103/physrevb.89.041407
- Medeiros, P. V. C., Tsirkin, S. S., Stafström, S., and Björk, J. (2015). Unfolding spinor wave functions and expectation values of general operators: Introducing the unfolding-density operator. *Phys. Rev. B* 91, 041116. doi:10.1103/physrevb.91.041116
- Migas, D. B., Shaposhnikov, V. L., Rodin, V. N., and Borisenko, V. E. (2010). Tungsten oxides. I. Effects of oxygen vacancies and doping on electronic and optical properties of different phases of WO<sub>3</sub>. *J. Appl. Phys.* 108, 093713. doi:10.1063/1.3505688
- Miyata, K., and Zhu, X. Y. (2018). Ferroelectric large polarons. *Nat. Mat.* 17 (5), 379–381. doi:10.1038/s41563-018-0068-7
- Momma, K., and Izumi, F. (2011). VESTA 3 for three-dimensional visualization of crystal, volumetric and morphology data. *J. Appl. Crystallogr.* 44, 1272–1276. doi:10.1107/s0021889811038970
- Niklasson, G. A., and Granqvist, C. G. (2007). Electrochromics for smart windows: Thin films of tungsten oxide and nickel oxide, and devices based on these. *J. Mat. Chem.* 17, 127–156. doi:10.1039/b612174h
- Perdew, J. P., Burke, K., and Ernzerhof, M. (1996). Generalized gradient approximation made simple. *Phys. Rev. Lett.* 77, 3865–3868. doi:10.1103/physrevlett.77.3865
- Pesci, F. M., Cowan, A. J., Alexander, B. D., Durrant, J. R., and Klug, D. R. (2011). Charge carrier dynamics on mesoporous WO<sub>3</sub> during water splitting. *J. Phys. Chem. Lett.* 2, 1900–1903. doi:10.1021/jz200839n
- Ping, Y., Rocca, D., and Galli, G. (2013). Optical properties of tungsten trioxide from first-principles calculations. *Phys. Rev. B* 87, 165203. doi:10.1103/physrevb.87.165203
- Regan, K. P., Koenigsmann, C., Sheehan, S. W., Konezny, S. J., and Schmuttenmaer, C. A. (2016). Size-dependent ultrafast charge carrier dynamics of WO<sub>3</sub> for photoelectrochemical cells. *J. Phys. Chem. C* 120, 14926–14933. doi:10.1021/acs.jpcc.6b04390
- Salje, E. K. H. (1994). *Eur. J. Solid State Inorg. Chem.* 31, 805.
- Salpeter, E. E., and Bethe, H. A. (1951). A relativistic equation for bound-state problems. *Phys. Rev.* 84, 1232–1242. doi:10.1103/physrev.84.1232
- Sangalli, D., Ferretti, A., Miranda, H., Attaccalite, C., Marri, I., Cannuccia, E., et al. (2019). Many-body perturbation theory calculations using the Yambo code. *J. Phys. Condens. Matter* 31, 325902. doi:10.1088/1361-648x/ab15d0
- Uemura, Y., Kido, D., Wakisaka, Y., Uehara, H., Ohba, T., Niwa, Y., et al. (2016). Dynamics of photoelectrons and structural changes of tungsten trioxide observed by femtosecond transient XAFS. *Angew. Chem. Int. Ed.* 55, 1364–1367. doi:10.1002/anie.201509252
- Uemura, Y., Uehara, H., Niwa, Y., Nozawa, S., Sato, T., Adachi, S., et al. (2014). *In situ* picosecond XAFS study of an excited state of tungsten oxide. *Chem. Lett.* 43, 977–979. doi:10.1246/cl.140144
- van Setten, M. J., Giantomassi, M., Bousquet, E., Verstraete, M. J., Hamann, D. R., Gonze, X., et al. (2018). The PseudoDojo: Training and grading a 85 element optimized norm-conserving pseudopotential table. *Comput. Phys. Commun.* 226, 39–54. doi:10.1016/j.cpc.2018.01.012
- Vogt, T., Woodward, P. M., and Hunter, B. A. (1999). The high-temperature phases of WO<sub>3</sub>. *J. Solid State Chem.* 144, 209–215. doi:10.1006/jssc.1999.8173
- Wang, F., Di Valentin, C., and Pacchioni, G. (2011). Electronic and structural properties of WO<sub>3</sub>: A systematic hybrid DFT study. *J. Phys. Chem. C* 115, 8345–8353. doi:10.1021/jp201057m
- Wang, W., Kang, Y., Peelaers, H., Krishnaswamy, K., and Van de Walle, C. G. (2020). 045116 First-principles study of transport in WO<sub>3</sub>. *Phys. Rev. B* 101, 045116. doi:10.1103/physrevb.101.045116
- Woodward, P. M., Sleight, A. W., and Vogt, T. (1995). Structure refinement of triclinic tungsten trioxide. *J. Phys. Chem. Solids* 56, 1305–1315. doi:10.1016/0022-3697(95)00063-1
- Yang, H., Sun, H., Li, Q., Li, P., Song, K., Song, B., et al. (2019). Structural, electronic, optical and lattice dynamic properties of the different WO<sub>3</sub> phases: First-principle calculation. *Vacuum* 164, 411–420. doi:10.1016/j.vacuum.2019.03.053
- Zheng, H., Ou, J. Z., Strano, M. S., Kaner, R. B., Mitchell, A., and Kalantar-zadeh, K. (2011). Nanostructured tungsten oxide - properties, synthesis, and applications. *Adv. Funct. Mat.* 21, 2175–2196. doi:10.1002/adfm.201002477